Energy & Environmental Science

ROYAL SOCIETY OF CHEMISTRY

PAPER

View Article Online
View Journal | View Issue

Cite this: *Energy Environ. Sci.*, 2025, **18**, 4241

Ultrathin cellulosic gel electrolytes with a gradient hydropenic interface for stable, high-energy and flexible zinc batteries†

Jichao Zhai,‡[a] Wang Zhao,‡[a] Lei Wang,*[a] Jianbo Shuai,[a] Ruwei Chen,[b] Wenjiao Ge,[a] Yu Zong,[a] Guanjie He *[b] and Xiaohui Wang *[a]

The increasing demand for personalized health monitoring has driven the development of wearable electronics. Flexible zinc-ion batteries (FZIBs) are ideal power sources for wearable devices, but their low volumetric energy densities have been a limitation for practical application. We present an ultrathin cellulose-based electrolyte (DCG) with a gradient hydropenic interface designed for stable and high-energy FZIBs to address this. The gradient hydropenic interface composed of deep eutectic solvent (DES) residuals effectively mitigates moisture-induced side reactions and guides planar zinc deposition. The resulting zinc anode with the ultrathin DCG shows 99.9% coulombic efficiency (CE) and a cycle life exceeding 4000 hours in symmetrical configuration. Under stringent conditions, including a 66% depth of discharge (DOD) and reduced DCG thickness (10 μm), the flexible zinc battery demonstrates stable cycling with energy densities of 222 W h kg^{-1} and 214.3 W h L^{-1} and successfully applied in wearable watches, offering performance comparable to lithium-ion batteries and outperforming previously reported zinc batteries.

Received 9th January 2025,
Accepted 13th March 2025

DOI: 10.1039/d5ee00158g

rsc.li/ees

Broader context

The rising demand for wearable electronics has spurred the advancement of next-generation energy storage devices. Flexible aqueous zinc-ion batteries (FZIBs) emerge as a promising alternative due to their high theoretical volumetric energy densities, which are often compromised by the substantial volume taken up by conventional homogeneous electrolytes. However, reducing the amount of these components presents challenges due to rapid consumption from side reactions at the interface between the electrolyte and the zinc anode, as well as uncontrolled zinc dendrite growth. In this study, we developed an ultrathin (10 μm) dual-network cellulose-based gel electrolyte (DCG) with a trace amount of gradient deep eutectic solvent (DES, 1 wt%) residues. This design effectively mitigates moisture-related side reactions and guides planar deposition with a preference for the 002 facet, significantly improving the reversibility of zinc anodes. As a result, FZIBs utilizing DCGs demonstrated excellent electrochemical performance, including high capacity, high coulombic efficiency, and stable cycling characteristics. The volumetric energy density of FZIBs with DCG was also enhanced, making them comparable to Li-ion and Na-ion batteries, thus showcasing their promising potential as power sources for wearable electronics.

Introduction

Wearable electronics are poised to be pivotal in the realm of personalized medicine, offering continuous and intimate monitoring of an individual's physical activities and health status.[1–3] The inherent flexibility and conformability of these devices make them an excellent foundation for the design of next-generation personalized wearable devices, opening new avenues for innovation and precision in health monitoring.[4,5] As the key component of power, the demand for flexible batteries with high energy densities and safety in wearable technology is imperative as these batteries ensure a comfortable, discreet fit, meet the energy requirements for continuous operation, prioritize user safety, and maintain durability.[6,7] It is believed that the volumetric energy densities of wearable batteries should be at least 100 W h L^{-1} (Medical Patch), considering further integration into wearable systems.[8]

Currently, lithium-ion batteries (LIBs) are the preferred energy source for portable electronics, electric vehicles, and

[a] State Key Laboratory of Pulp and Paper Engineering, School of Light Industry Science and Engineering, South China University of Technology, Guangzhou City, Guangdong Province, 510640, China. E-mail: felwang@scut.edu.cn, fewangxh@scut.edu.cn
[b] Department of ChemistryUniversity College London, 20 Gordon Street, London, WC1H 0AJ, UK. E-mail: g.he@ucl.ac.uk

† Electronic supplementary information (ESI) available. See DOI: https://doi.org/10.1039/d5ee00158g

‡ These authors contributed equally to this work.

drones due to their high energy density and excellent cycling performance.[9,10] However, traditional LIBs lack flexibility, mainly because of the rigidity of their cell components.[11] To overcome this limitation, researchers have developed a diverse range of flexible batteries (FBs) over the past decade, leveraging both conventional LIB materials and innovative battery technologies, such as lithium-metal and aqueous batteries.[12,13] Among these, evolution in the aqueous system has drawn special attention due to its inherent exceptional safety.[14]

Wearable aqueous zinc-ion batteries (ZIBs) are ideal power sources for wearable devices due to the advantages of Zn metal anodes, including unbeatable theoretical capacity (5855 mA h cm^{-3}), low redox potential (−0.76 V *vs.* SHE), and abundant reserves.[15,16] However, zinc anodes suffer from several problems, such as uncontrollable dendrite growth, rampant hydrogen evolution reaction (HER), and corrosion, resulting in poor reversibility, low coulombic efficiency (CE), and ineluctable electrolyte consumption.[17,18] Various strategies, including the design of current collectors and separators,[19,20] construction of artificial solid electrolyte interfaces (SEIs),[21–23] and the modification of electrolytes,[24–26] have been adopted to solve these problems. Compared with the other strategies, which involve relatively complex preparation processes, electrolyte engineering is relatively simple and convenient to protect Zn anodes. Among all the electrolytes, semi-solid hydrogel electrolytes not only help fix water molecules to alleviate side reactions but also mitigate leakage during operation, holding great potential for practical application in wearable ZIBs.[27,28] Currently, the gel electrolytes are homogeneously structured. Their preparation involves dissolving the gel network's constituent materials in solvents, followed by solidification and solvent removal, a cycle often repeated multiple times before immersing the cleaned gel in an electrolyte solution.[29,30] Their poor reversibility and mechanical properties constrain the reduction of the hydrogel electrolyte thickness (>100 μm) and the amount of Zn (depth of discharge, DOD < 10%) involved in the full cell usually, compromising the energy densities of wearable ZIBs.[31,32] Currently, the volumetric energy density of the ZIBs was only ∼70 W h L^{-1}, well below that of the lithium counterpart.[33]

Herein, we report an ultrathin cellulose-based hetero gel electrolyte with solvent residues designed for stable and high-energy wearable zinc batteries. The dual-network cellulose-based gel electrolyte (DCG), which features a rapid Zn^{2+} transport channel due to polar coordination, was prepared through a dissolution–regeneration procedure. In this process, trace amounts of deep eutectic solvent (DES, mixture of 3-amino-1-propanol and 1-allyl-2,3,4,6,7,8-hexahydropyrrolo[1,2-*a*]pyrimidin-1-ium chloride, DBNACl 1 wt%) remained in the gel as a functional additive (Fig. S1–S3, ESI†). Compared to other homogeneously structured gel electrolytes, these DESs in our DCG can migrate to the surface of the zinc anode under the influence of an electric field, effectively displacing moisture in the local environment and mitigating side reactions. Meanwhile, the DES can passivate the (002) plane, thereby regulating the nucleation and deposition direction of Zn metal along the (002) direction, effectively eliminating dendrite growth and improving reversibility. Consequently, the zinc anode with the ultrathin DCG exhibited an exceptional CE of 99.9%, achieving an ultralong cycle life (>4000 hours) in a Zn‖Zn symmetrical configuration. Under the strict limitations of excess Zn (66% DOD) and a reduced thickness of DCG, a flexible zinc battery composed of paper electrodes can deliver stable cycling with satisfactory energy densities (222 W h kg^{-1} and 214.3 W h L^{-1}), reaching levels comparable to non-aqueous Li-ion counterparts at the device level and outperforming previously reported zinc batteries. This technology was further successfully applied in wearable watches.

Results

Construction of the ultrathin DCG electrolyte with gradient DES residuals

The ultrathin DCG was prepared through a straightforward dissolution–regeneration process of cellulose fibers (Fig. 1a). Initially, the cellulose fibers were dissolved in DES and subsequently regenerated in a bath containing zinc salt (refer to the Experimental section for details, Fig. S4, ESI†). A trace amount of DES (1%) remained in the gel (Fig. S5, ESI†), which featured a dual interaction network consisting of hydrogen bonding among cellulose molecules as well as coordination bonds between Zn cations and cellulose (Fig. S6, ESI†).[34] Due to the coordination of Zn^{2+} with the free hydroxyl groups of cellulose, the gel provides rapid hopping pathways for the zinc cations (Fig. S7, ESI†). Being assembled into a full cell, the DES migrates to the surface of the Zn anode, thereby displacing water near the electrode and enhancing reversibility by alleviating related side reactions. For comparison, full cells were also assembled using the liquid electrolyte (LE) and the cellulose gel (CG) regenerated in water.

The dual network was formed during the regeneration after introducing the zinc salt in the composite. By incorporating 1.5 mol L^{-1} $Zn(OTf)_2$ in the matrix, the peak at 3438 cm^{-1} corresponding to the stretching vibration of the hydroxide radicals for the original cellulose gel shifted to the 3490 cm^{-1}, confirming the coordination effect of Zn cations with cellulosic chains (Fig. 1b). To highlight this point, the Raman spectra reveal that both cellulose and CG exhibit an −OH peak around 3000 cm^{-1} (see Fig. S8, ESI†). In contrast, our DCG displays a significant shift corresponding to the hydroxyl radical at 2890 cm^{-1}, which is consistent with the results from the Fourier transform infrared (FTIR) spectrum. This additional evidence further confirms the coordination between Zn cations and cellulose. This dual network further greatly enhances the mechanical properties of the gel electrolyte and thus can form an ultrathin free-standing gel film (10 μm, Fig. S9, ESI†), which can be further processed into a round disk (Fig. 1c). This small disk can be either twisted or bent at a small radius (<1 mm, insert in Fig. 1c), exhibiting good flexibility. The dual molecular network can form and leave interconnected voids inside the flexible matrix (Fig. 1d),

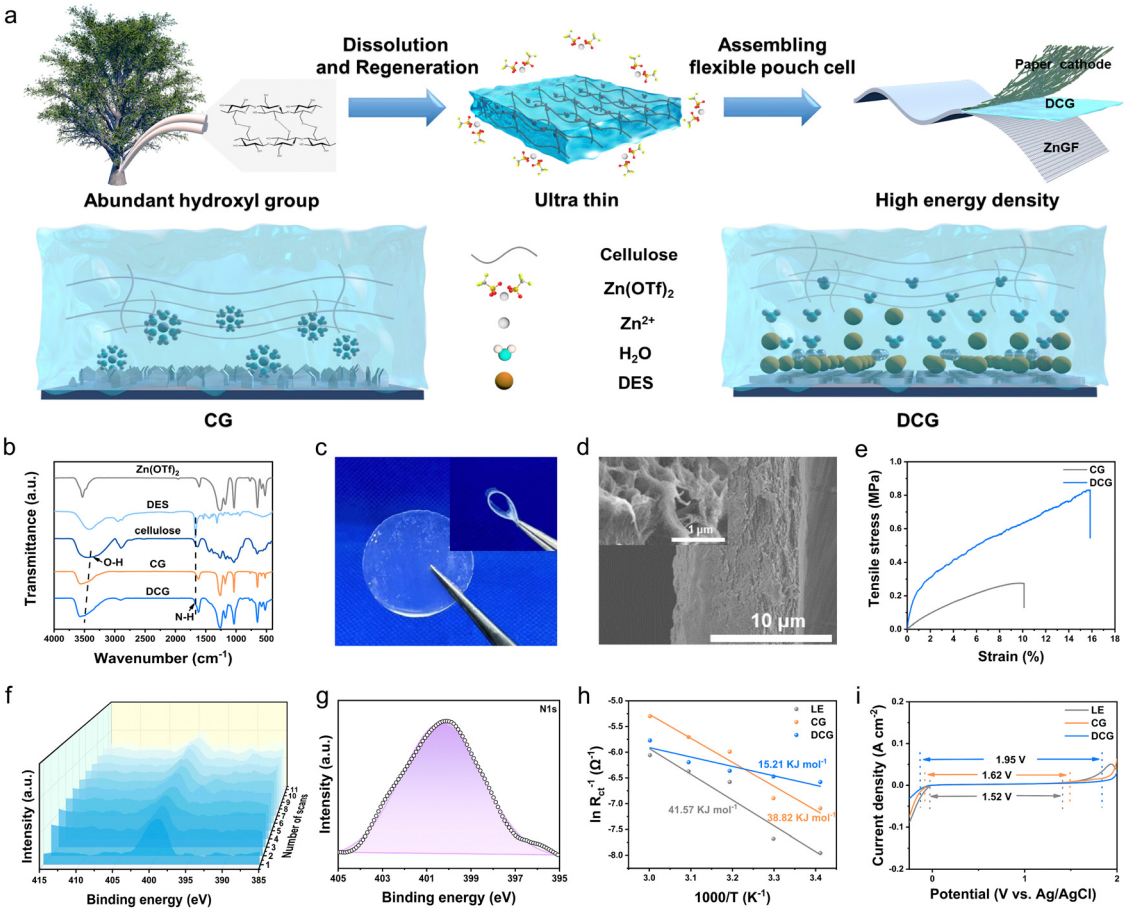

Fig. 1 Construction of the ultrathin DCG electrolyte with gradient DES residuals. (a) Illustration of the preparation of DCG and the multiple interactions within it. (b) FTIR spectra of $Zn(OTf)_2$, cellulose, CG and DCG. (c) Photographs of normal and bending of DCG. (d) Cross-sectional scanning electron microscope (SEM) image of DCG. (e) The mechanical properties of DCG and normal cellulose gel. (f) The Ar^+ Etch XPS N 1s spectra of DCG in the Zn‖Zn battery after 20 cycles. (g) XPS N 1s spectra of the Zn anode in the Zn‖Zn battery after 20 cycles. (h) Arrhenius curves and the corresponding desolvation activation energies. (i) The overall ESW of different electrolytes at 1 mV s^{-1}.

facilitating rapid transporting pathways for both Zn cations and DES residuals. Compared with the pristine cellulose gel regenerated in water, the tensile strength of the DCG is four times higher, which can be ascribed to the additional network structure by the crosslinking between the cellulose and Zn cations (Fig. 1e). Compared to recently published gel electrolytes of different polymers, DCG is superior in thickness, ionic conductivity and tensile strength (Fig. S10, ESI†).[28,30,35–37] During the regeneration, a trace amount (1%) of the DES remained in the matrix, which further migrates to the surface of the zinc anode under the electric field in the subsequent cycles because of the positive charges in the DES (Fig. S11, ESI†), further constructing the gradient interface near the zinc anode (N element in the DES, Fig. 1f) due to the space occupying effect.[38] In the meantime, these DES traces can effectively passivate the surface of the zinc anode by firmly binding the surface (Fig. 1g).

It should be noted that DES residuals in the gel electrolyte can bind the zinc cations (Fig. S12, ESI†), interrupting the solvation structure, further decreasing the activation energy and facilitating the rapid transfer of the zinc cations at the electrode–electrolyte interface. As a proof of concept, the gel electrolyte without DES residuals (cellulosic gel, CG) was the control sample prepared *via* water regeneration as CG was immersed in a $Zn(OTf)_2$ aqueous solution. We evaluated the ability of Zn^{2+} to desolvate structures at the electrode electrolyte interface by measuring the electrochemical impedance spectroscopy (EIS) characterization of Zn‖Zn batteries at various temperatures (Fig. S13, ESI†) and calculating the activation energy (E_a) according to the Arrhenius equation. The E_a value of 15.21 kJ mol^{-1} for the DCG containing DES was significantly lower than those of CG (38.82 kJ mol^{-1}) and LE (41.57 kJ mol^{-1}), suggesting that DES facilitates the desolvation process of Zn/Zn^{2+} for the rapid transfer of Zn^{2+} (Fig. 1h).[39] As shown in Fig. S14 and S15 (ESI†), the transference number of Zn^{2+} for DCG (1.13) is significantly higher than that of CG (0.87) and LE (0.84), demonstrating the exceptional Zn^{2+} transport capability of the gradient DES interface. Additionally, the locally gradient DES residual can displace water near the zinc and thus alleviate the side reaction associated with moisture. As shown in Fig. 1i, the electrochemical stability window (ESW) of DCG can reach 1.95 V, much larger than those of the CG (1.62 V) as well as the

liquid electrolyte (1.52 V), potentially enhancing the reversibility of the zinc anode.[40]

Theoretical investigation of functions of the gradient DES interface

We have conducted the theoretical investigations to further explore the potential of the ultrathin DCG in protecting the zinc anode. The interaction between the DES traces and the zinc anode was first studied. It is observed that the adsorption energy between DES and each Zn crystal plane is higher than those between H_2O and the corresponding crystal planes (Fig. 2a), indicating that DBNACl in locally gradient DES can repel water from the surface of zinc and alleviate the side reaction. Additionally, molecular dynamics (MD) simulations further demonstrate that the stable adsorption of DES on the Zn surface prevents H_2O from reaching the Zn anode (Fig. 2b). This effectively avoids side reactions and enhances the ESW of the batteries, which is consistent with the aforementioned ESW results.

The zinc salt was subsequently induced in the system to clarify the preferred orientation of the zinc deposition in two systems (Fig. 2c). The adsorption energy of DES on Zn(002) (−8.35 eV) is lower than that on Zn(100) (−11.34 eV) and Zn(101) (−10.89 eV) crystal planes. This DES can firmly be absorbed on the zinc anode through bonding between the polar functional groups (N atoms in the hydrogen bond acceptor as well as –OH and –NH in the hydrogen bond donor, Fig. 2d) and zinc metal. According to the Bravais law, the orientation of crystal planes is determined by the ion deposition rate on different planes, with the lowest growth rate leading to the final exposed crystal plane.[41,42] Therefore, this low binding energy suggests that the (002) plane is less constrained, causing Zn ions to diffuse to the (100) and (101) planes and then deposit. Consequently, the deposition rate of Zn^{2+} on the Zn(002) plane is the lowest, leaving the Zn(002) structure exposed. In sharp contrast, similar adsorption energies of Zn^{2+} on the three crystal planes in the pure $Zn(OTf)_2$/cellulose gel electrolyte system were observed, indicating the randomly orientated deposition of zinc. This orientated deposition can further render a dendrite-free morphology of the zinc anode, which was further validated by COMSOL multiphysics field simulations. In the DES-containing system (Fig. 2e), 3-amino-

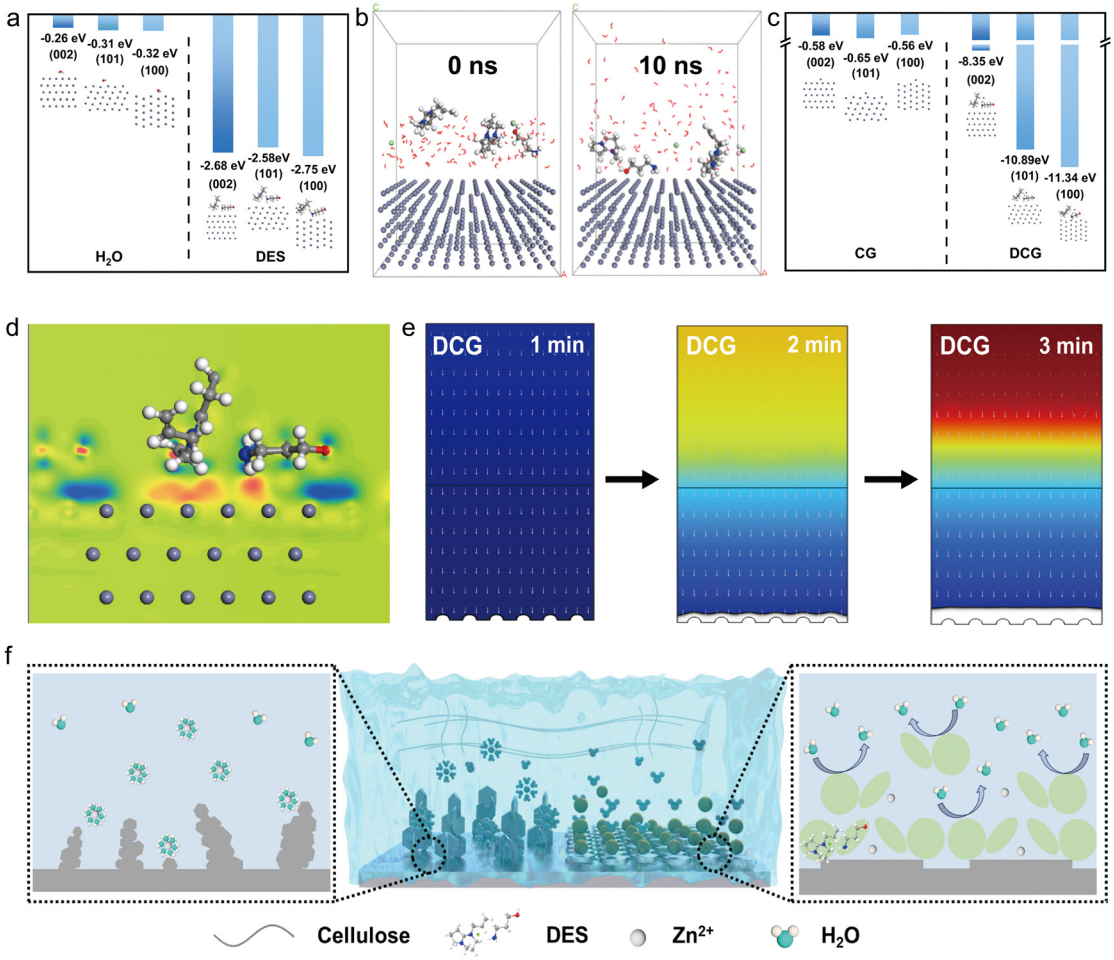

Fig. 2 Theoretical investigation of functions of the gradient DES interface on the Zn anode. (a) The adsorption energy of DES and H_2O on the Zn(002), (100), (101) surface. (b) The MD simulation for understanding the effect of the water environment on DES/Zn interaction. (c) Adsorption energy of Zn^{2+} on DES and Zn anode adsorbed crystal planes. (d) The differential charge density of DES on the Zn(002) crystal plane. (e) The COMSOL simulation results of Zn dendrite growth in DCG. (f) The schematic diagrams of the bare Zn anode and Zn with DCG in plating/stripping cycles.

1-propanol induces uniform nucleation and promotes a uniform distribution of the Zn^{2+} flux, resulting in uniform Zn deposition. Conversely, in the pure $Zn(OTf)_2$/cellulose gel electrolyte system, the Zn^{2+} aggregated at the most favorable nucleation sites on the Zn metal, where they nucleate and continuously deposit, resulting in a tip effect and the formation of dendrites (Fig. S16, ESI†).[43]

In summary, the gradient DES traces in the DCG can improve the reversibility of the zinc anode in following ways (Fig. 2f). DES adsorption energies on zinc crystal planes are higher than those of water, and DBNACl repels water and mitigates side reactions, which further prevents water from reaching the zinc anode, enhancing the ESW of the batteries. In addition, DES traces have a lower adsorption energy on the Zn(002) plane, and attraction of Zn^{2+} by 3-amino-1-propanol promotes preferential zinc deposition on (100) and (101) planes, leading to an exposed (002) structure and dendrite-free morphology. COMSOL simulations validated that the DCG induces uniform Zn nucleation and flux distribution in the matrix, resulting in uniform zinc deposition. All in all, cellulose works synergistically with DES to rapidly transport Zn^{2+}, guide its planar deposition, and protect the anode, thereby reducing the occurrence of side reactions.

Side-reaction alleviation and planar deposition of Zn in the DCG

As discussed above, the gradient DES interface can alleviate dendrite growth by facilitating the planar deposition of Zn (Fig. 3a). As a proof of the concept, we examined the *in situ* deposition behavior of Zn under various electrolytes using *in situ* optical microscopy at a practical current density of 2 mA cm^{-2} (Fig. 3b). Notably, the Zn anode exhibited a uniform and thin deposition layer devoid of dendrites and bubbles even after 60 minutes with DCG, demonstrating DCG's superior performance in suppressing side reactions and promoting Zn planar deposition. In contrast, zinc anodes immersed in LE and CG suffered from severe dendrite growth and bubble formation, which can be attributed to side reactions including the hydrogen evolution reaction.

We further compared the deposition processes, including nucleation and growth, by evaluating the diffusional model with chronoamperometry (CA) tests (Fig. 3c). When a constant

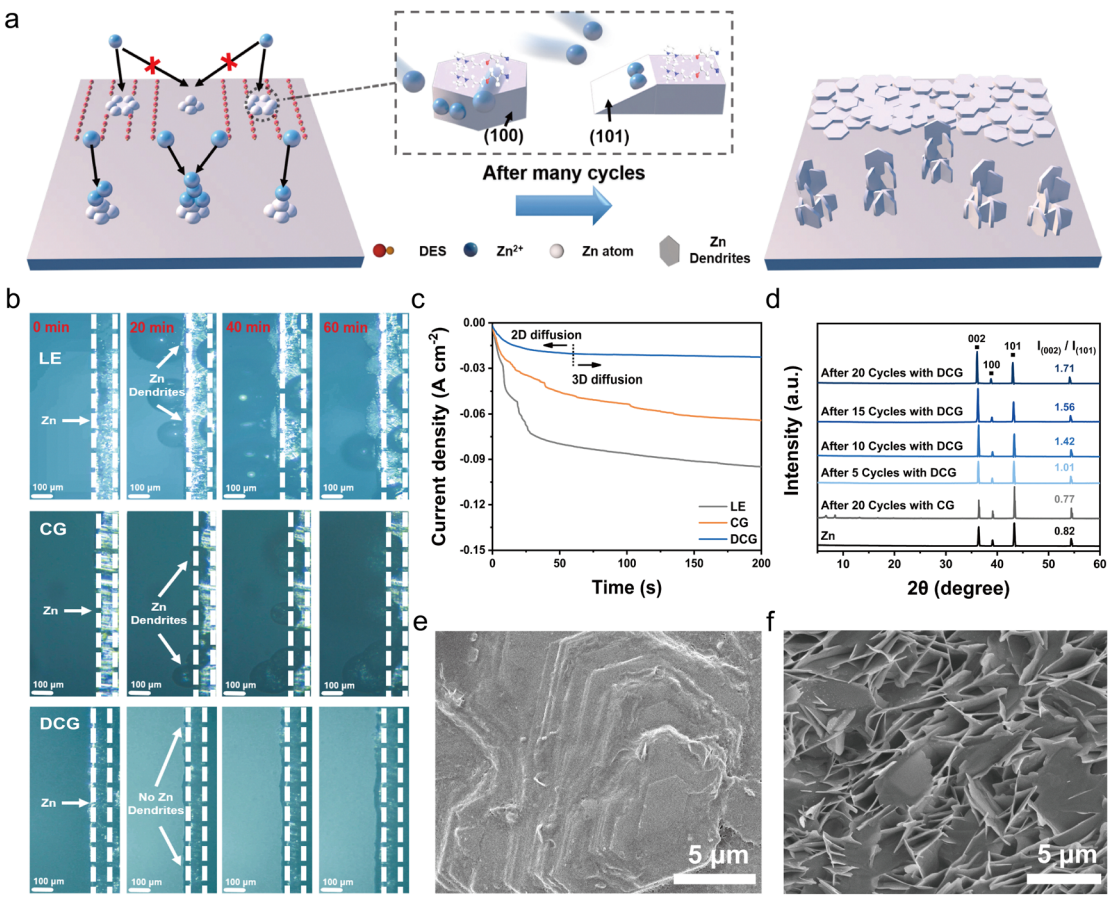

Fig. 3 Side-reaction alleviation and planar deposition of Zn in DCG. (a) The schematic diagrams for Zn deposition in different electrolytes. (b) *In situ* optical images of Zn metal during the plating process with LE, CG, and DCG. (The scale bar in the figure represents 100 μm). (c) The CA curves for LE, CG and DCG. (d) XRD patterns of Zn foils at the pristine state and the deposited states after cycling in the Zn‖Zn batteries for 20 cycles with CG and different numbers of cycles (5, 10 and 20) with DCG. The SEM images of the Zn metal after plating for 20 cycles with (e) DCG and (f) CG.

voltage of 150 mV was applied, the current density increased rapidly over time with LE, indicating a prolonged two-dimensional diffusional process of Zn dendrite formation, lasting more than 300 s. In the case of CG, the 2D diffusion still required an extended duration. However, DCG exhibited a brief 2D diffusion phase in the first 60 seconds, followed by stable 3D diffusion with a significantly smaller steady-state current. This reduced period of constrained 2D diffusion can decrease the local accumulation of zinc cations, thereby reducing the possibility of dendrite formation.[44,45]

We conducted *ex situ* X-Ray diffraction (XRD) to further confirm the planar deposition of zinc with DCG (Fig. 3d). The peak intensity ratio (002)/(101) on the Zn surface with CG after 20 cycles was only 0.77, lower than that of the pristine Zn foil (0.82), indicating dendrite growth. In contrast, the Zn surface with DCG showed no significant by-products in the XRD plots, suggesting that the side reaction was alleviated. Notably, the peak intensity ratio of (002)/(101) increased significantly from 1.01 to 1.71 after 20 cycles, suggesting that Zn(002) growth was dominant with DCG, resulting in a more uniform electrodeposited Zn surface. In addition, XPS F 1s spectra reveal the emergence of the by-products on the Zn anode with CG after 20 cycles (1.54%, shown in Fig. S17, ESI†). However, no discernible by-products on the Zn anode were detected in the DCG system, further demonstrating the successful inhibition of the side reaction during the deposition.

This planar deposition is further evidenced by the morphologies after cycling. After 20 cycles, hexagon-shaped Zn plates with a layered structure can be observed with the DCG electrolyte, corresponding to the Zn(002) crystal plane, which parallels the Zn substrate (Fig. 3e and Fig. S18, ESI†). In contrast, with LE and CG under the same conditions, sharp dendrites are clearly observed on the Zn metal (Fig. 3f and Fig. S19 and S20, ESI†), further demonstrating excellent performance of DCG in suppressing side reactions and promoting Zn planar deposition (Fig. S21, ESI†). To more accurately evaluate the effect of DCG on smoothing the deposition process, we conducted atomic force microscopy (AFM) testing to measure the average roughness of the zinc negative electrode surface. We analyzed the zinc anode after 20 cycles using DCG, LE, and CG under a current density of 1 mA cm^{-2} and a discharge capacity of 1 mA h cm^{-2}. The results are presented in Fig. S22 (ESI†). Notably, the AFM images indicate that the average surface roughness of the charged zinc anode with LE is 161 nm, while that with CG is 121 nm. In contrast, the anode with the DCG electrolyte exhibits a significantly lower roughness of only 41 nm, which is approximately three to four times less than that of the LE and CG anodes. These findings highlight the excellent capability of DCG in regulating Zn deposition, which is further supported by the complementary results from both SEM and AFM analyses.

To further illustrate the universal adaptability of this function across different electrolytes, we incorporated DES into various liquid electrolytes (LEs) containing different salts, such as $ZnSO_4$, $Zn(OTF)_2$, and $ZnCl_2$, since $ZnSO_4$ cannot form a stable gel electrolyte with cellulose. After 20 cycles, hexagon-shaped Zn plates with a layered structure were observed in the LEs containing DES, corresponding to the Zn(002) crystal plane and aligning with the Zn substrate (see Fig. S23a, c and e, ESI†). In contrast, sharp dendrites were clearly visible on the Zn metal in symmetric batteries using electrolytes that lack DES (see Fig. S23b, d and f, ESI†). These findings robustly demonstrate that the beneficial effects of DES on the deposition of Zn particles are applicable to batteries utilizing electrolytes with various salts, further highlighting the positive impact of DES on Zn deposition.

Enhanced reversibility of the Zn anode in DCG

The planar deposition and alleviated side reaction in the DCG can greatly enhance the reversibility of the zinc anode. As a proof of concept, the Zn‖Cu asymmetric battery with DCG sustained a high average CE of over 99.9% (after first cycle, Fig. 4a) in more than 700 cycles under a current density of 1 mA cm^{-2}. In sharp contrast, the CE of the Zn‖Cu asymmetric battery with LE dropped to 40% after 280 cycles (average 96.1%). This decreased CE can be attributed to significant side reactions and dendrite growth. Notably, the initial CE of DCG was 97%, significantly higher than LE (89%) and CG (91%), demonstrating DCG's superior ability to inhibit side effects from the onset (Fig. 4b). Furthermore, the corrosion and side reactions of various electrolytes on the zinc anode were evaluated using the linear polarization resistance (LPR) test (Fig. 4c).[46] The corrosion potential of DCG (−0.94 V) was higher than that of LE (−0.98 V) and CG (−0.96 V), and its corrosion current was lower, indicating a lower corrosion rate and tendency on the Zn anode, which further implies that DCG can enhance the cycling stability of Zn batteries.

The cycling stability of the zinc anode with DCG was further evaluated in the Zn‖Zn symmetric batteries with the thin zinc metal (30 μm). The symmetric batteries with DCG demonstrated a long-term cycling life span for more than 4000 hours, maintaining a stable polarization voltage (70 mV) at 4 mA cm^{-2} and 4 mA h cm^{-2}. As the controlling sample, Zn‖Zn symmetric batteries using LE and CG electrolytes experienced short-circuiting after 200 h and 432 h with much larger overpotentials (240 mV, 80 mV), respectively. We further disassembled the cell after cycling to check whether the gel electrolyte was penetrated. DCG remained intact without any dendritic crystal residues on the surface (Fig. S24a, ESI†), while many dark spots can be clearly observed on the CG after 200 cycles due to short-circuiting (Fig. S24b, ESI†), which further demonstrates the outstanding dendritic inhibition of the DCG. To further explore the potential of the DCG in the high-energy batteries under large areal capacity, we cycled the symmetrical cell at a high current density of 30 mA cm^{-2} and a high areal capacity of 30 mA h cm^{-2}. The cell with DCG operated stably for over 300 h, which outperformed the cell with LE and CG electrolytes (Fig. S25, ESI†). This excellent cycling stability should be firmly associated with a stable interface, which can be demonstrated by the variation of the interfacial transfer resistance (R_{ct}) in the EIS tests of the Zn‖Zn symmetric batteries. After 1000 cycles, the R_{ct} value of the cell remained a stable value of 565 Ω compared with that in the initial cycle (580 Ω). In

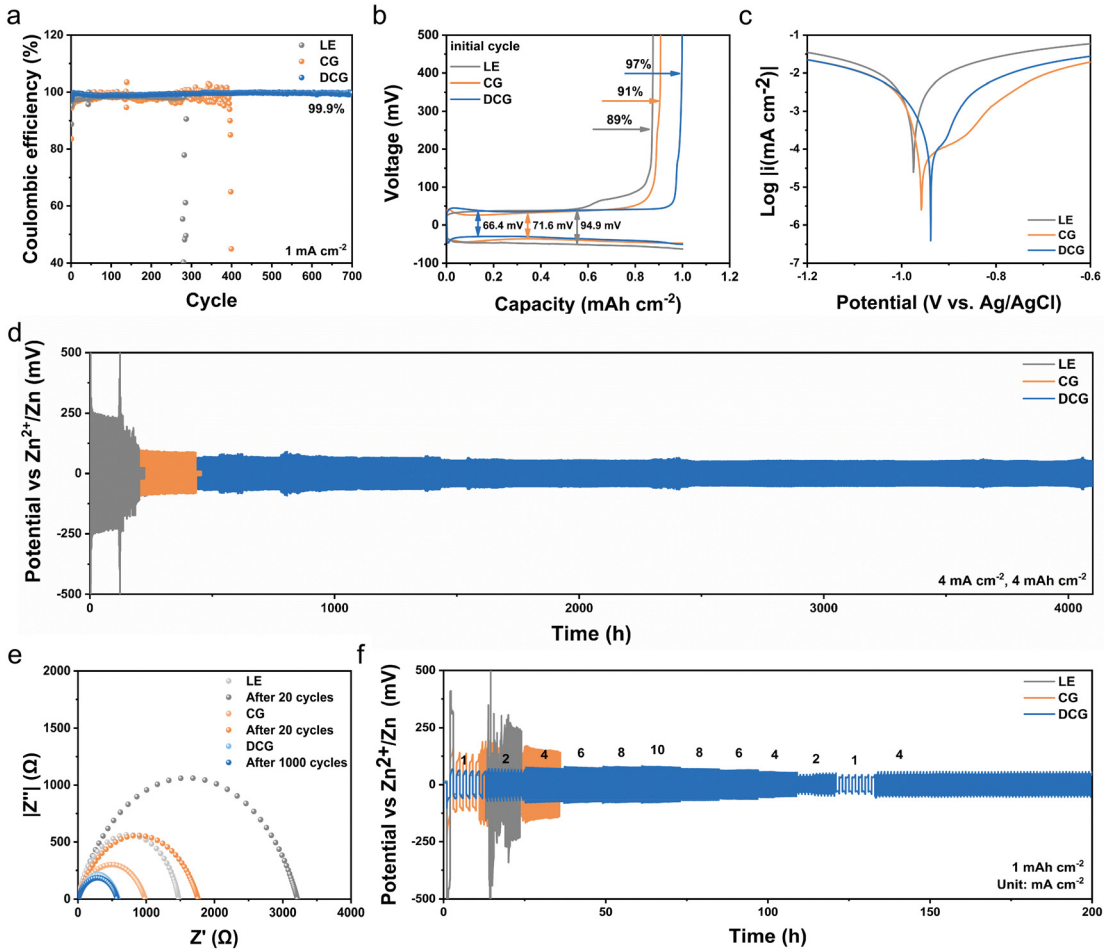

Fig. 4 Evaluation of the electrochemical performance of the Zn anode with the DCG electrolyte. (a) The CE performance of the asymmetrical Zn||Cu battery with LE, CG and DCG under 1 mA cm^{-2} and (b) the corresponding initial cycle profiles. (c) The LPR curves for LE, CG and DCG. (d) The performance of the Zn||Zn battery with LE, CG and DCG under 4 mA cm^{-2} and 4 mA h cm^{-2}. (e) EIS curves of the Zn||Zn battery with LE, CG (after 20 cycles) and DCG (after 1000 cycles). (f) Rate performance of the symmetrical Zn battery with LE, CG and DCG.

great contrast, the R_{ct} values of the CG increased from the 980 Ω to 1750 Ω, demonstrating a deteriorative Zn/electrolyte interface.

The enhanced ionic conductivity of zinc cations in the DCG enables the superior rate capability of the symmetrical cells. As a proof of concept, we cycled the symmetrical cells under a varied current density. The cell with DCG exhibited stable overpotentials of 60, 65, 70, 75, 78 and 82 mV at the current densities of 1, 2, 4, 6, 8 and 10 mA cm^{-2}, respectively. When the current returned to 4 mA cm^{-2}, the cell with DCG showed a flat and stable galvanostatic charge/discharge (GCD) profile during the cycling, while the control samples showed sharply increased overpotentials (Fig. 4f).

Building high-energy and flexible battery with ultrathin DCG

The low overpotential and high stability of symmetrical cells with DCG offer significant advantages in constructing high-energy-density flexible zinc batteries. To demonstrate this, we paired a flexible zinc textile anode (ZnGF, Fig. S26, ESI†) and a V_2O_5 paper cathode (Fig. S27–S29, ESI†) to assemble the full cell (Fig. 5a and Fig. S30, ESI†). The flexibility of these electrodes is shown in Fig. S31 (ESI†). The oversized Zn in the full cell was kept under 50% to ensure high energy density.

Our DCG exhibited excellent compatibility with the V_2O_5 cathode. The full cell with DCG showed the same number of redox peaks in the cyclic voltammetry (CV) curves (Fig. S32, ESI†) as the control sample, indicating identical redox processes of the paper cathode with different electrolytes. Considering the enhanced reversibility of the zinc anode, the full cell with DCG could be stably cycled for over 1000 cycles with an exceptional capacity retention of 85.2% (Fig. 5b). In contrast, the batteries based on LE and CG failed after 630 and 811 cycles, respectively. In the meanwhile, the voltage gaps between the oxidation and reduction reactions in the cell with DCG were much smaller (Fig. 5c), likely due to enhanced ionic conductivity and kinetics. This improved kinetics can enhance the utilization of active materials in the cathode, leading to increased capacity, as reflected in the enlarged area of the CV curves and higher specific capacity in the full cell. As a proof of concept, the Zn||V_2O_5 battery with DCG exhibited a high reversible capacity of up to 418.6 mA h g^{-1} at 1 A g^{-1}, far exceeding

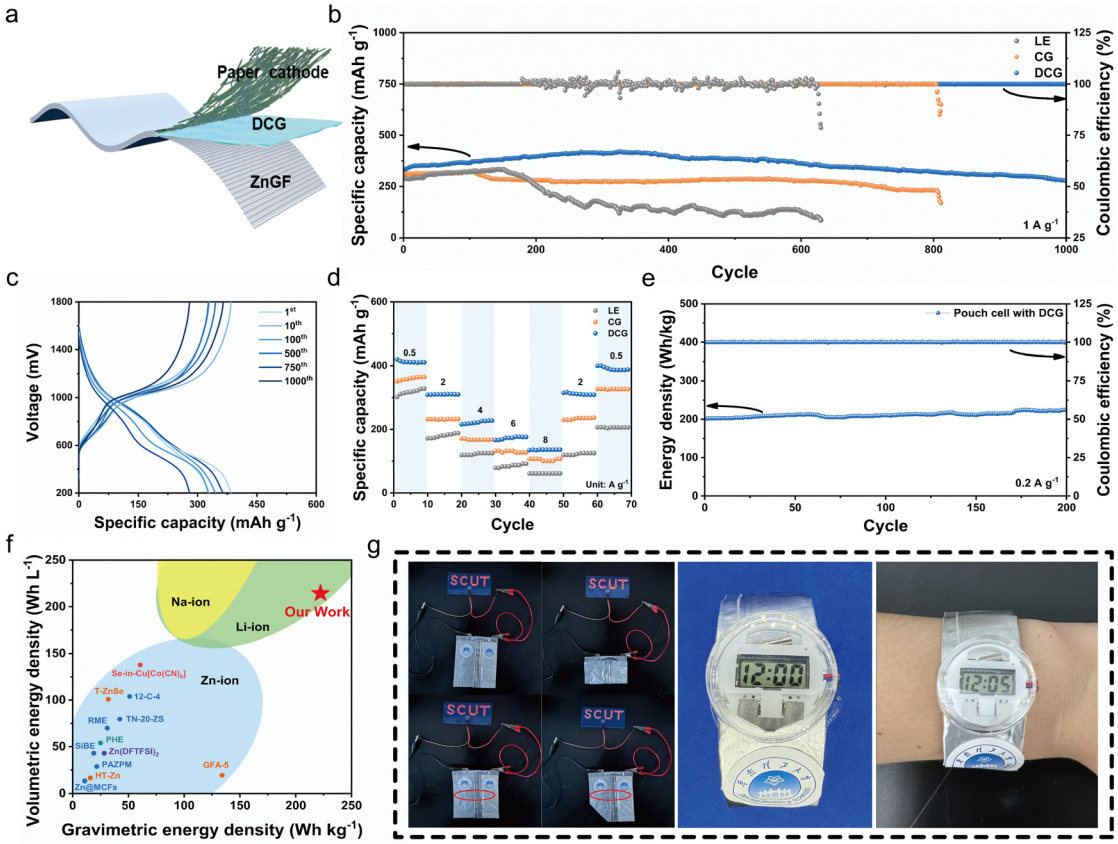

Fig. 5 Evaluation and practical application of the high energy flexible Zn cell based on DCG. (a) The schematic illustration of the flexible Zn‖V_2O_5 pouch cell with DCG. (b) The long-term cycling performance of the Zn‖V_2O_5 battery with LE, CG and DCG (the cycling test was conducted within a voltage window of 0.2 to 1.8 V at a current density of 1 A g^{-1}, with the mass loading of V_2O_5 being approximately 5 mg cm^{-2}). (c) The selected GCD curves of the Zn‖V_2O_5 battery with DCG at 1 A g^{-1}. (d) The rate performance of the Zn‖V_2O_5 battery with DCG. (e) Cycling performance of the flexible Zn‖V_2O_5 pouch cell with DCG at 0.2 A g^{-1}. (f) The pouch cell performance comparison between our developed flexible Zn‖V_2O_5 batteries with previously reported Zn battery technologies in terms of volumetric energy density *versus* gravimetric energy density. (g) Practical applications of flexible Zn‖V_2O_5 pouch cells with DCG for powering LEDs and a digital watch.

those with LE (322.2 mA h g^{-1}, Fig. S33a, ESI†) and CG (331.7 mA h g^{-1}, Fig. S33b, ESI†).

Beyond excellent cycling stability, the full cell with our DCG also exhibited improved rate capability. Batteries based on DCG showed capacities of 411.2, 310.5, 226.4, 173.4, and 136.2 mA h g^{-1} at current densities of 0.5, 2, 4, 6, and 8 A g^{-1} (Fig. S34, ESI†), respectively, much higher than those with other electrolytes (Fig. 5d). When the current density was restored to 0.5 A g^{-1}, the capacity recovered to 387 mA h g^{-1}. This improved rate capability can be attributed to higher ion mobility and lower charge transfer resistance (R_{ct}, EIS, Fig. S35, ESI†).

To further explore the practical potential for wearable applications, we prepared a flexible Zn‖V_2O_5 pouch cell. Considering the low mass fraction of the inactive electrolyte in the pouch, the flexible cell exhibited an impressive energy density of 222 W h kg^{-1} for stable cycling over 200 cycles (Fig. 5e). The ultrathin nature of the pouch cell also provided an excellent volumetric energy density of 214.3 W h L^{-1}, offering a significant advantage over other zinc batteries and potentially serving as alternatives to Li-ion and Na-ion counterparts (Fig. 5f).

For further practical applications, two flexible Zn‖V_2O_5 pouch cells connected in series successfully powered 39 light-emitting diodes (LEDs) arranged in the "SCUT" pattern. The LED array maintained its luminance even after being bent, punctured, or sheared, with no flames or thermal runaway observed, demonstrating high safety. To further illustrate the capability of flexible Zn‖V_2O_5 pouch cells in powering flexible electronic products, we assembled two series-connected pouch cells into a strap as a single power source for an electronic watch, which lasted over 12 hours. The improved energy density and outstanding safety of the full cell with DCG underscore its practical potential in various wearable electronic devices (Fig. 5g).

Conclusions

In summary, we designed an ultrathin cellulose-based electrolyte with a gradient hydropenic interface designed to enhance the stability and energy density of wearable zinc batteries. The dual-network cellulose-based gel electrolyte (DCG), created

through a dissolution–regeneration process, features rapid Zn^{2+} transport channels enabled by coordination. During synthesis, trace amounts of deep eutectic solvent (DES, 1 wt%) are retained as a functional additive. This DES migrates to the zinc anode surface under an electric field, displacing moisture and forming a gradient hydropenic interface that mitigates side reactions. Additionally, the DES passivates the (002) plane, directing Zn metal deposition along this plane to prevent dendrite growth and improve reversibility. Consequently, the zinc anode with the ultrathin DCG demonstrates a coulombic efficiency (CE) of 99.9% and an ultralong cycle life exceeding 4000 hours in a Zn‖Zn symmetrical configuration. Under stringent conditions, including limited excess Zn and a reduced DCG thickness, a flexible zinc battery with paper electrodes delivers stable performance and achieves energy densities of 222 W h kg^{-1} and 214.3 W h L^{-1}, which are on par with non-aqueous Li-ion batteries and surpass those of previously reported zinc batteries. This technology has been successfully applied in wearable watches, highlighting its potential for broader application in wearable electronics.

Author contributions

L. W. and X. H. W. conceived the project and supervised the research. J. C. Z. and J. B. S. prepared the materials. J. C. Z., W. Z., J. B. S., R. W. C. and W. J. G. conducted the characterization and analyzed the data. W. Z. performed molecular simulation. J. C. Z., L. W., Y. Z., X. H. W. and G. J. H. wrote the paper and all authors engaged in discussions related to the manuscript.

Data availability

The data that support the findings of this study are available from the corresponding author upon reasonable request.

Conflicts of interest

There are no conflicts to declare.

Acknowledgements

This work was financially supported by the Guangdong Basic and Applied Basic Research Foundation (2023B1515040013 and 2024A1515010678), the National Natural Science Foundation of China (22308109, 52103109 and U23A6005), the State Key Laboratory of Pulp & Paper Engineering (2023ZD01, 2023C02, and 2024ZD02) and the Fundamental Research Funds for Central Universities (2023ZYGXZR093). This work was supported by the Engineering and Physical Sciences Research Council (EPSRC, EP/V027433/3), UK Research and Innovation (UKRI) under the UK Government's Horizon Europe funding (101077226 and EP/Y008707/1). This work was partially supported by the High Performance Computing Platform of South China University of Technology.

References

1 W. Liu, M.-S. Song, B. Kong and Y. Cui, *Adv. Mater.*, 2017, **29**, 1603436.
2 J. D. MacKenzie and C. Ho, *Proc. IEEE*, 2015, **103**, 535–553.
3 Z. Su, Y. Yang, Q. Huang, R. Chen, W. Ge, Z. Fang, F. Huang and X. Wang, *Prog. Mater. Sci.*, 2022, **125**, 100917.
4 L. Ren and B.-W. Zhang, *Exploration*, 2022, **2**, 20210182.
5 H. Li, P. Tan, Y. Rao, S. Bhattacharya, Z. Wang, S. Kim, S. Gangopadhyay, H. Shi, M. Jankovic, H. Huh, Z. Li, P. Maharjan, J. Wells, H. Jeong, Y. Jia and N. Lu, *Chem. Rev.*, 2024, **124**, 3220–3283.
6 C. Li, L. Li, B. He, Y. Ling, J. Pu, L. Wei, L. Sun, Q. Zhang and Y. Yao, *Mater. Sci. Eng., R*, 2022, **148**, 100671.
7 B. Dai, X. Shi, X. Pei, F. Xu and Y. Zhao, *Energy Storage Mater.*, 2024, **66**, 103231.
8 J. Chang, Q. Huang and Z. Zheng, *Joule*, 2020, **4**, 1346–1349.
9 Y. Xia, L. Wang, X. Li, T. Liao, J. Zhai, X. Wang and K. Huo, *Battery Energy*, 2024, **3**, 20240015.
10 C.-Y. Park, J. Kim, W.-G. Lim and J. Lee, *Exploration*, 2024, **4**, 20210255.
11 L. Li, Q. Zhang, B. He, R. Pan, Z. Wang, M. Chen, Z. Wang, K. Yin, Y. Yao, L. Wei and L. Sun, *Adv. Mater.*, 2022, **34**, 2104327.
12 D. Zhao, Z. Li, D. Xu and Z. Yang, *Adv. Funct. Mater.*, 2024, **34**, 2316182.
13 S. Wen, C. Luo, Q. Wang, Z. Wei, Y. Zeng, Y. Jiang, G. Zhang, H. Xu, J. Wang, C. Wang, J. Chang and Y. Deng, *Energy Storage Mater.*, 2022, **47**, 453–461.
14 X. Geng, X. Hou, X. He and H. J. Fan, *Adv. Energy Mater.*, 2024, **14**, 2304094.
15 K. Zhu, X. Niu, W. Xie, H. Yang, W. Jiang, M. Ma and W. Yang, *Energy Environ. Sci.*, 2024, **17**, 4126–4136.
16 X. Zhao, Y. Gao, Q. Cao, F. Bu, J. Pu, Y. Wang and C. Guan, *Adv. Energy Mater.*, 2023, **13**, 2301741.
17 Q. Yang, Q. Li, Z. Liu, D. Wang, Y. Guo, X. Li, Y. Tang, H. Li, B. Dong and C. Zhi, *Adv. Mater.*, 2020, **32**, e2001854.
18 J. Yan, E. H. Ang, Y. Yang, Y. Zhang, M. Ye, W. Du and C. C. Li, *Adv. Funct. Mater.*, 2021, **31**, 2010213.
19 Z. Hao, Y. Zhang, Y. Lu, J. Hou, X. Liu, Z. Yan and J. Chen, *Adv. Funct. Mater.*, 2024, **34**, 2315726.
20 L. Yang, Y.-J. Zhu, H.-P. Yu, Z.-Y. Wang, L. Cheng, D.-D. Li, J. Tao, G. He and H. Li, *Adv. Energy Mater.*, 2024, 2401858.
21 L. Miao, Z. Guo and L. Jiao, *Energy Mater.*, 2023, **3**, 300014.
22 N. Xu, C. Yuan, G. Sun, N. Chen, S. Yao and F. Du, *Carbon Neutrality*, 2023, **2**, 33.
23 X. Cai, W. Wu, B. Zhang, W. Cai, C. Lu, R. Xiong, J. Zhao and J. Zhou, *Energy Environ. Sci.*, 2025, DOI: **10.1039/D5EE00202H**.
24 T. Fang, M. Wu, F. Lu, Z. Zhou, Y. Fu and Z. Shi, *Energy Mater.*, 2024, **4**, 400039.
25 R. Chen, C. Zhang, J. Li, Z. Du, F. Guo, W. Zhang, Y. Dai, W. Zong, X. Gao, J. Zhu, Y. Zhao, X. Wang and G. He, *Energy Environ. Sci.*, 2023, **16**, 2540–2549.
26 X. Li, Z. Chen, P. Ruan, X. Hu, X. Yuan, B. Lu, L. Qin and J. Zhou, *Nanoscale*, 2024, **16**, 18835–18842.

27 M. Jiao, L. Dai, H.-R. Ren, M. Zhang, X. Xiao, B. Wang, J. Yang, B. Liu, G. Zhou and H.-M. Cheng, *Angew. Chem., Int. Ed.*, 2023, **62**, e202301114.
28 Z. Shen, Y. Liu, Z. Li, Z. Tang, J. Pu, L. Luo, Y. Ji, J. Xie, Z. Shu, Y. Yao, N. Zhang and G. Hong, *Adv. Funct. Mater.*, 2024, 2406620.
29 Z.-J. Chen, T.-Y. Shen, X. Xiao, X.-C. He, Y.-L. Luo, Z. Jin and C.-H. Li, *Adv. Mater.*, 2024, 2413268.
30 K. Chen, J. Huang, J. Yuan, S. Qin, P. Huang, C. Wan, Y. You, Y. Guo, Q. Xu and H. Xie, *Energy Storage Mater.*, 2023, **63**, 102963.
31 R. Qin, Y. Wang, L. Yao, L. Yang, Q. Zhao, S. Ding, L. Liu and F. Pan, *Nano Energy*, 2022, **98**, 107333.
32 J. Yang, B. Yin, Y. Sun, H. Pan, W. Sun, B. Jia, S. Zhang and T. Ma, *Nano-Micro Lett.*, 2022, **14**, 42.
33 H. Zhou, C. Liu, J.-C. Wu, M. Liu, D. Zhang, H. Song, X. Zhang, H. Gao, J. Yang and D. Chen, *J. Mater. Chem. A*, 2019, **7**, 9708–9715.
34 H. Zhang, X. Gan, Y. Yan and J. Zhou, *Nano-Micro Lett.*, 2024, **16**, 106.
35 Z. Meng, Y. Jiao and P. Wu, *Angew. Chem., Int. Ed.*, 2023, **62**, e202307271.
36 Y. Cheng, Y. Jiao and P. Wu, *Energy Environ. Sci.*, 2023, **16**, 4561–4571.
37 H. Tian, M. Yao, Y. Guo, Z. Wang, D. Xu, W. Pan and Q. Zhang, *Adv. Energy Mater.*, 2024, 2403683.
38 M. Fang, B. Du, X. Zhang, X. Dong, X. Yue and Z. Liang, *Angew. Chem., Int. Ed.*, 2024, **63**, e202316839.
39 H. Zhang, X. Gan, Z. Song and J. Zhou, *Angew. Chem., Int. Ed.*, 2023, **62**, e202217833.
40 G. Li, Z. Zhao, S. Zhang, L. Sun, M. Li, J. A. Yuwono, J. Mao, J. Hao, J. Vongsvivut, L. Xing, C.-X. Zhao and Z. Guo, *Nat. Commun.*, 2023, **14**, 6526.
41 M. Qiu, P. Sun, Y. Wang, L. Ma, C. Zhi and W. Mai, *Angew. Chem., Int. Ed.*, 2022, **61**, e202210979.
42 T. Wei, Y. Ren, Y. Wang, L. E. Mo, Z. Li, H. Zhang, L. Hu and G. Cao, *ACS Nano*, 2023, **17**, 3765–3775.
43 L. Li, Y. Zheng, J. Xu, B. Peng, G. Zhu, J. Wu, L. Ma and Z. Jin, *ACS Energy Lett.*, 2024, **9**, 3269–3289.
44 K. Zhao, G. Fan, J. Liu, F. Liu, J. Li, X. Zhou, Y. Ni, M. Yu, Y.-M. Zhang, H. Su, Q. Liu and F. Cheng, *J. Am. Chem. Soc.*, 2022, **144**, 11129–11137.
45 T. Wei, Y. Ren, Y. Wang, L. Mo, Z. Li, H. Zhang, L. Hu and G. Cao, *ACS Nano*, 2023, **17**, 3765–3775.
46 Y. Wang, T. Wang, S. Bu, J. Zhu, Y. Wang, R. Zhang, H. Hong, W. Zhang, J. Fan and C. Zhi, *Nat. Commun.*, 2023, **14**, 1828.

